Electrification Mechanism and Constituted Near-electrode Layer inside Electrostatic Atomizers

Babak Kashir, Anthony Perri, Alexander L. Yarin, Farzad Mashayek*
Department of Mechanical and Industrial Engineering, University of Illinois at Chicago,
842 W. Taylor St., Chicago, Illinois, United States
*Corresponding author: mashayek@uic.edu

Abstract

The electrification mechanism inside the electrostatic atomizers and the constituted layer adjacent to the electrode are investigated numerically. The formation of the polarized diffuse layer across the electrode and inside the atomizer is studied through an appropriate, realistic model. This model accounts for the discharge of the counter-ions at the interface of the diffuse and compact layers through well-known faradaic reactions. These reactions at the interface are taken into account through Frumkin-Butler-Volmer kinetics equation derived from our previous experimental measurements. Fixed flux boundary conditions for the ions predict the concentrations at the interface of the diffuse and compact layers and inside the diffuse layer. The computational domain starts from the interface of the compact and diffuse layers and extends toward the bulk flow region inside the electrostatic atomizer. The components of the ionic transport equation are studied in a sample two-dimensional micro-channel configuration. The numerical solver is developed within the OpenFOAM platform and is previously validated through the available numerical benchmarks.

Keywords

Electrification mechanism; Electrostatic atomizers; High voltage

Introduction

Electrostatic atomization systems are considered as an attractive option for terrestrial and aerial applications due to the higher efficiency of atomization, especially in the case of highly viscous fluids [1]. These systems provide enhanced spray dispersion and higher controllability of spray trajectory [2,3]. Also, they avoid problems of customary injection systems such as uneven or over-application of oil droplets. The suitable fluids for electrostatic atomizers are poorly conducting liquids which provide enhanced charge residence time in contrast to conducting liquids.

Poorly conducting liquids in the scope of electrohydrodynamic phenomena are described as leaky dielectric liquids which are fundamentally different than the perfect dielectrics [4]. Their small electric conductivity values allow them to possess a small amount of net charge. Liquids such as transformer oils, refrigerants, and various organic solvents lie within the concept of poorly conducting liquids or weak electrolytes in the framework of electrochemistry [5]. The model put forward by Taylor [4], Melcher & Taylor [6] and later by Saville [7] elaborates some hydrodynamic phenomena of the application of electric fields to such liquids by charge transport in them. In these applications such as the electrostatic atomization, ions are considered as the charge carriers.

In electrostatic atomizers, electrodes are metals acting as perfect conductors (iso-potential conductors) [8]; which can sustain electric current and impose zero tangential electric fields [9,10]. Irreversible faradaic reactions take place at the surface of the metallic electrodes inside electrostatic atomizers [11]. The kinetic-limited regime (rather than the diffusion-limited) faradaic reactions are responsible for the electrification of poorly conducting liquids in these atomizers. In the kinetic-limited regime, the electric current is regulated kinetically by the reaction rate rather than by the supply rate from the diffusion. Ions are discharged and become neutralized, or neutral species are charged and become ions through these sustained faradaic reactions. The kinetics of these reactions follow the well-known Frumkin-Butler-Volmer equation in electrochemistry [12,13].

The Frumkin-Butler-Volmer kinetic-based nature of faradaic reactions at the electrode surface composes distinct layers including the compact and diffuse layers [14,15]. The imposed electric potential at the electrode surface has a major role in the creation of these layers. In ionic conductors, such as water, a compact layer is formed by ionic crowding at the surface of the electrode due to the high electrode potential [15]. However, in poorly conducting electrolytes such as vegetable oils, which are of interest in the current study, ion crowding is not deemed as the dominant mechanism. In such liquids, the non-specific (non-electric) adsorption is known as the causing mechanism [16].

The previous computational studies on electrification inside electrostatic atomizers are based on charge injection theory [17,18]. In this approach, a single transport equation is solved for the charge density inside the computational domain [19]. The experimentally observed and measured electric current density and counter-ion flux do not play a direct role in the presented models. However, they propose methods to estimate the magnitude of the charge at the electrode surface as a fixed value. This estimation provides a Dirichlet-type boundary condition instead of accounting for the faradic reactions. None of the previous studies accounted for the electrification mechanism inside the electrostatic atomizers. Taking a closer look at the near-electrode constituted layers and the formation circumstances of these layers provide valuable information on the mechanism of creation of charge carriers in poorly conducting liquids and facilitate development of computational models that predict the performance of the electrostatic atomizers.

The first work considering ionic flux boundary conditions due to the faradaic reactions at the electrode surface is performed by Bazant et al. [20,21]. However, these works were for low voltage electrochemical cells of aqueous solutions with low flux values at the electrode surface. The applied potentials at the electrodes in electrostatic atomizers are multiple orders of magnitude higher than the conventional electrochemical cells. Moreover, the electrolyte is composed of poorly conducting liquids (for instance, vegetable oils) rather than the strong conducting electrolytes.

The present work predicts the poorly conducting liquids electrification in contact with the conducting electrodes (metals) carrying a sustained electric current which is the common case in electrostatic atomizers. Also, we demonstrate the constituted near-electrode polarized diffuse layer which is predicted through the numerical simulations. Realistic conditions inside the electrostatic atomizers are taken into account through appropriate ionic-flux boundary conditions accounting for the discharge of counter-ions at the electrode surface through the faradaic reactions.

Governing equations

The Open Field Operation and Manipulation (OpenFOAM) C++-based library is used as the computational platform to build and develop the required numerical tools [22]. The governing equations for the electrohydrodynamic flow of poorly conducting liquids inside the electrostatic atomizers include the continuity, momentum, ionic transport, and the Poisson equations.

The incompressible fluid flow governing equations including the continuity and momentum equations are as follows:

$$\nabla \cdot \mathbf{V}_* = 0 \tag{1}$$

$$\rho_* \left[\frac{\partial \mathbf{v}_*}{\partial t_*} + (\mathbf{V}_* \cdot \nabla)\mathbf{V}_* \right] = -\nabla p_* + \mu \nabla^2 \mathbf{V}_* + q_* \mathbf{E}_* + q_* \mathbf{E}_{*\text{ext}} \tag{2}$$

Here, * marks the dimensional variable. $\mathbf{V}_*$ is the velocity field vector; ρ_* is the density; t_* is the time and p_* indicates the pressure. $q_* = e(c_*^+ - c_*^-)$ is the bulk charge density with c_*^+ and c_*^- being the cation and anion concentrations, respectively, and e the elementary charge. $\mathbf{E}_* = -\nabla\varphi_*$ identifies the electric field imposed by the self-induced electric potential (φ_*) inside the atomizer through imbalanced ion concentrations. $\mathbf{E}_{*\text{ext}}$ refers to the externally applied electric field (in case of presence). It is important to note that the last two terms in the momentum equation describe the Coulombic body force related to the presence of net charge due to the polarization in the near-electrode layers.

Also, the cation and anion transport equations and the Poisson equation addressing the self-induced electric potential are as follows, respectively:

$$\frac{\partial c_*^+}{\partial t_*} + \nabla \cdot (c_*^+ \mathbf{V}_*) = D\nabla^2 c_*^+ + \frac{De}{k_B T} \nabla \cdot (c_*^+ \nabla\varphi_*) \tag{3}$$

$$\frac{\partial c_*^-}{\partial t_*} + \nabla \cdot (c_*^- \mathbf{V}_*) = D\nabla^2 c_*^- - \frac{De}{k_B T} \nabla \cdot (c_*^- \nabla\varphi_*) \tag{4}$$

$$\nabla^2 \varphi_* = -\frac{q_*}{\varepsilon \varepsilon_0} \tag{5}$$

where k_B is the Boltzmann constant; T is the temperature and D is the diffusivity coefficient. Also, ε is the relative permittivity and ε_0 indicates the vacuum permittivity.

In this paper, the electrohydrodynamic flow case of canola oil is considered, which has been concurrently studied experimentally by the present group [10,11]. The electric conductivity of canola oil is measured to be $\sigma = 2.6 \times 10^{-11}$ Sm^{-1} . The relative dielectric permittivity ε is taken to be 3. This yields the charge relaxation time $\tau_c = \varepsilon\varepsilon_0/\sigma$ equal to 1 s. The diffusion coefficient of canola oil is reported to be $D = 10^{-11}$ m^{2}s^{-1} in room temperature [23]. This provides the Debye screening length to be $\lambda_D = (D\tau_c)^{1/2} = 3.16$ μm.

The bulk ion concentration $(c_{*\infty})$ is calculated to be in the order of 10^{17} m^{-3} from the following relation [24]:

$$c_{*\infty} = \frac{\varepsilon\varepsilon_0 k_B T}{2e^2 \lambda_D^2} \tag{6}$$

The numerical solver has been previously validated through distinct one- and two-dimensional benchmarks [25,26] and provides a reliable ground to study the electrohydrodynamic flow of canola oil inside the electrostatic atomizers.

The concurrent experimental measurements of canola oil have provided an electric current-voltage relation for the discharge of counter-ions at the electrode surface [10,11] considering the Frumkin-Butler-Volmer kinetics as:

$$J_{e*} = j_{0*}10^{\left\{\left(-\frac{V_{0*}}{2}+\psi_1\right)/b_c\right\}} = 10^{\left\{\left(-\frac{V_{0*}}{2}-(a_c-\psi_1)\right)/b_c\right\}} \left[\frac{A}{cm^2}\right] \tag{7}$$

where j_{0*} is the exchange current density, $-V_{0*}/2$ is the applied voltage at the cathode, $a_c - \psi_1$ and b_c are the experimentally measured coefficients equal to -291,83.0 V and -3,451.85 V, respectively.

Results and discussions
Here, we consider the two-dimensional case of an electrohydrodynamic flow inside a microchannel with an active electrode section. The microchannel consists of three parts including the inlet, electrode and exit sections. Figure 1 represents the considered configuration for the microchannel and the constituting sections. The considered sample case mimics the electrode section and the insulating parts in real electrostatic atomizers. Although the presence of insulating parts at both before and after locations with regard to the electrode section might depend on the particular design of the electrostatic atomizer.
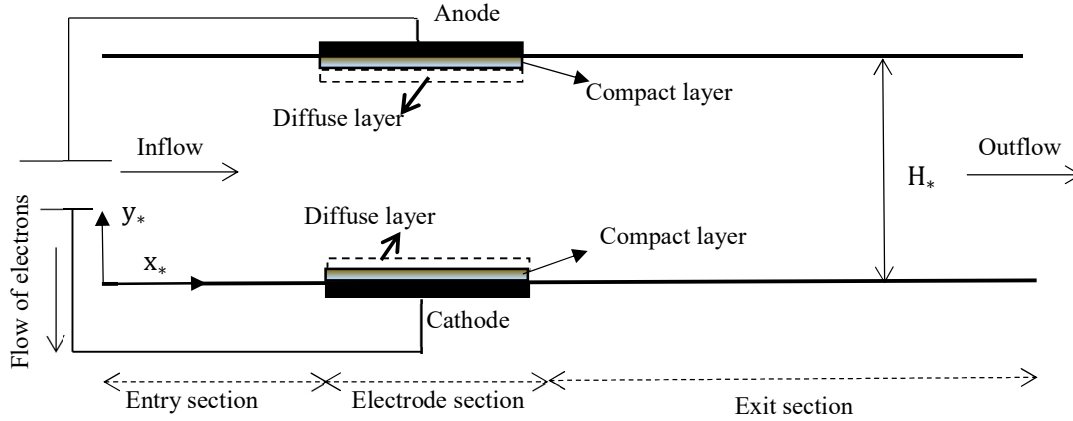

Figure 1. Considered configuration with the opposite polarity electrodes and insulated entry and exit sections. The compact and diffuse layers are also depicted.

A fully-developed pressure-driven laminar flow with a maximum velocity of 0.004 ms^{-1} is considered as the inflow. The entry and electrode sections are considered to be 6 µm, and the exit section's length is 96 µm. The channel height is 20 µm. The Reynolds number, defined based on the maximum inlet velocity and the half-channel height, is 0.0005. No-slip boundary condition is imposed for the velocity along the channel walls. The entry and exit sections are fully insulated with no faradaic reactions or any non-specific adsorption (i.e. $dc_*^-/dy_* = dc_*^+/dy_* = 0$). The middle part (active electrodes) sustain electric current due to the faradaic reactions and is connected to batteries. The ion flux values at the electrode surface, where the convective term vanishes, are found through employing relation (7) which accounts for the Butler-Volmer-Frumkin kinetics at the electrode surface. The computational boundary at the electrodes starts from the interface of the compact and diffuse layers.
The definition of flux without the convective term yields:

$$j_*^{\pm} = -D\frac{dc_*^{\pm}}{dy_*} \mp \frac{De}{k_BT}c_*^{\pm}\frac{d\varphi_*}{dy_*} \tag{8}$$

The cations flux at the anodic interface (between the compact and diffuse layers) vanishes, whereas at the cathodic interface it is determined by the connected battery as j_*^+. These conditions provide the following boundary conditions for the cations at the cathodic and anodic interfaces:

$$\frac{dc_*^+}{dy_*} = -\frac{e}{k_BT}c_*^+\frac{d\varphi_*}{dy_*} \qquad \text{(anode)} \tag{9}$$

$$\frac{dc_*^+}{dy_*} = -\frac{j_*^+}{D} - \frac{e}{k_BT}c_*^+\frac{d\varphi_*}{dy_*} \qquad \text{(cathode)} \tag{10}$$

Similarly, the anion boundary conditions at the cathodic and anodic interfaces are as:

$$\frac{dc_*^-}{dy_*} = -\frac{j_*^-}{D} + \frac{e}{k_BT}c_*^-\frac{d\varphi_*}{dy_*} \qquad \text{(anode)} \tag{11}$$

$$\frac{dc_*^-}{dy_*} = \frac{e}{k_BT}c_*^-\frac{d\varphi_*}{dy_*} \qquad \text{(cathode)} \tag{12}$$

Due to the similar boundary conditions, the cation and anion fluxes are equal i.e. $|j_*^-| = |j_*^+|$. Hence, the ion fluxes are found through concurrent experimental measurements (Eq. (7)) as $|j_*^-| = |j_*^+| = J_{e*}/e$. The applied potentials at the electrodes are considered to be ±500 V. This yields the ion fluxes to be 3.1×10^{14} m^{-2} s^{-1}.

Situated between the electrode surface and the polarized diffuse layer is a thin compact layer, which has been described by theoretical models. The model proposed by Stern [16] considers a dielectric surface with a non-zero ζ-potential without sustaining an electric current. A mono-layer of non-specifically adsorbed ions create the compact layer in the seminal work of Stern. Liquids with the relative dielectric permittivity close to 1 experience almost all of the potential drop across the compact layer, while in liquids with high relative dielectric permittivity ($\varepsilon \gg 1$) the major part of the potential drop occurs across the diffuse layer [21]. Based on the relative dielectric permittivity of canola oil liquid ($\varepsilon_{canola} = 3$), we estimated 99% percent of the potential drop to occur across the compact layer. Hence, the electric potential at the interface of the compact and diffuse layers is assumed to be 5 V.

Two different grids are considered to provide results independent of the grid resolution. The considered grid resolutions are indicated in Table 1. The cells length in x_* direction, cell heights at the wall and the center of the channel and also the total number of grid points are denoted by Δx_*, Δy_{*wall}, $\Delta y_{*center}$ and n_{tot}, respectively.

Table 1. Grid specifications for the simulations of the electrohydrodynamic flow.

Grid	Δx_* (nm)	Δy_{*wall} (nm)	$\Delta y_{*center}$ (nm)	n_{tot}
Coarse	67	3.94	78	2592000
Fine	60	3.4	69	3240000

The results obtained based on the two grids are in agreement and no further grid refinement was considered. Moreover, further local coarsening of grid cells close to the electrode produced inaccurate numerical predictions (numerical overshooting occured). In the following, the results based on the fine grid are presented and discussed.

Figure 2 provides the two-dimensional contours of anions and cations distribution in the computational domain. Strong repulsion of co-ions from the electrodes is obvious in this figure (blue color). Slight accumulation (red color in the magnified view) of counter-ions at the vicinity of the electrodes is also observed. This accumulation results as the outcome of the competition between the attraction of counter-ions due to the electro-migration and the discharge of counter-ions due to the faradaic reactions occurring at the interface of the compact and diffuse layers.
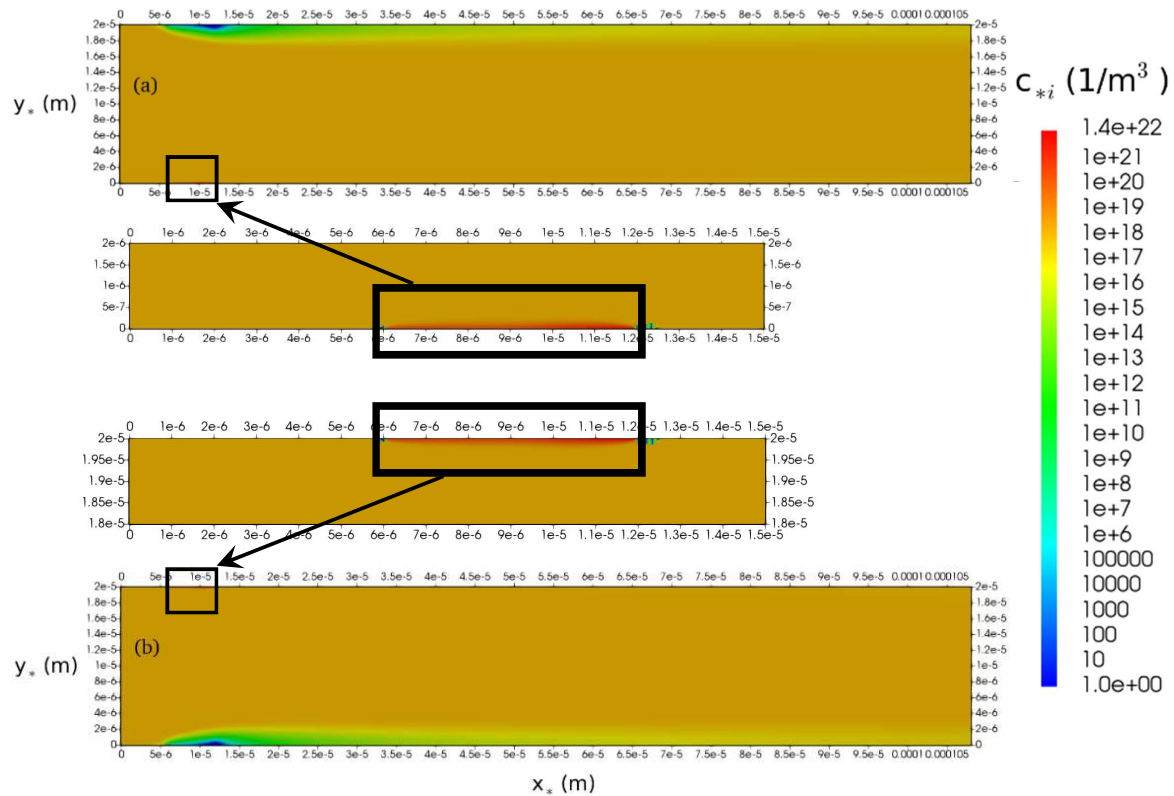

Figure 2. Two-dimensional contours of ions in the electrohydrodynamic flow of canola oil inside a microchannel exposed to opposite-polarity electrodes. (a) Cation concentrations and (b) anion concentrations.

The dimensionless cation concentration along the channel and in different vertical positions are shown in Fig. 3. Here and hereinafter, the half-channel height ($h_* = 10$ μm) and bulk ion concentration ($c_{*\infty} = 8 \times 10^{17}$ m^{-3}) are the employed scales to provide dimensionless values for the coordinates (x_* and y_*) and ion concentrations (c_*^- and c_*^+), respectively.
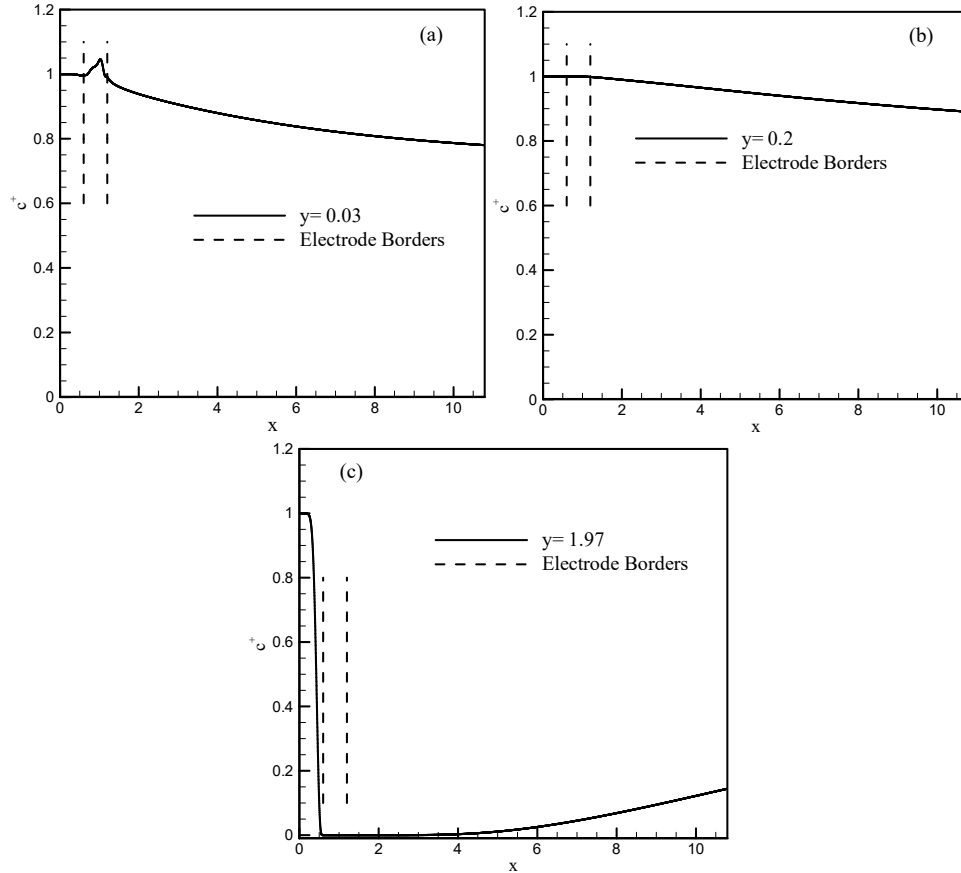
Figure 3. Dimensionless cation concentration along the channel and in different vertical positions.

(a) y= 0.03, (b) y= 0.2, (c) y= 1.97.

In Fig. 3, at y = 0.03 and for the locations between the electrode borders, an increase in the cation concentration is observed. This implies that the attraction of cations through the electromigration process is greater than the consumption of cations through discharge at the cathodic interface, which results in this accumulation in the vicinity of the cathode surface. At lower-half vertical positions, i.e. y ∈ {0.03,0.2}, and after the electrode section, the cation concentration tends to decrease. This can be explained by the diffusion of cations from the lower half to the upper half of the channel. Diffusion tends to balance the cation concentration at the exit section of the channel. The gradual increase of cation concentration at y= 1.97 and after the electrode section can be interpreted by a similar argument. The strong repulsion of cations from the anode (upper electrode) is obvious in Fig. 3(c) which shows a void region even after the electrode section up to x= 4 locations.

We define the thickness of the diffuse layer (λ_d) as the vertical distance from the interface of the compact and diffuse layers (the starting point of the computational domain near the electrodes) to the position where the absolute net charge drops to 1% of its maximum value at the interface, i.e., to $0.01e(c_*^+ - c_*^-)|_{int.}$. Figure 4 provides the thickness of the diffuse layer along the cathode (the lower half electrode). Due to the symmetry, we expect the same values of diffuse layer thickness for the anode (the upper half electrode). It is seen in Fig. 4 that the effect of the border edges of the electrode section and the insulated walls provides a concave distribution for the diffuse layer profile. It is expected that the diffuse layer thickness distribution includes a more flattened profile by increasing the electrode section.

In Fig. 1, the exit section is considered long enough to track the components of the ionic balance terms present in Eqs. (3-4) at far downstream locations. The ionic transport equations include the convective, electro-migrative and the diffusive terms. Due to the symmetric boundary conditions, the results for the cation balance terms on the lower half of the channel resemble the results for the anions on the upper half. Hence, only the cation transport equation

terms are investigated along the exit section of the channel at different vertical positions. The scale $\tau_c/c_{*\infty} = (8 \times 10^{17})^{-1}$ [m^{3}s] is utilized to provide the convective $\nabla \cdot (c_*^+ \mathbf{V}_*)$, electro-migrative $(De/k_B T)\nabla \cdot (c_*^+ \nabla \varphi_*)$ and the diffusive terms $D\nabla^2 c_*^+$ dimensionless. It is important to recall that the y-component of the convective term is absent in the channel flow with a spanwise velocity profile.
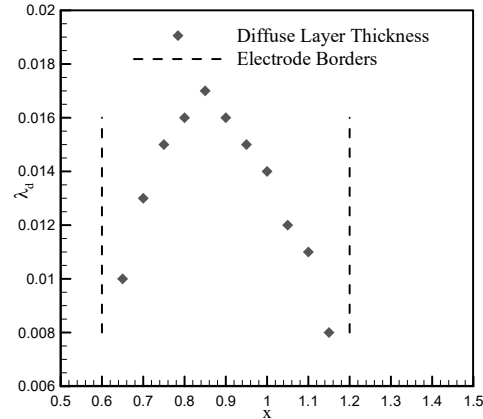

Figure 4. Diffuse layer thickness inside the electrode section (lower half) for the two-dimensional microchannel flow case

Three different vertical positions are considered to plot the dimensionless components of the cation transport equation in downstream locations after the electrode section. The first and last positions are at the vicinity of the upper and lower walls, while the second position is farther away from the lower wall and still in the lower half of the channel (y= 0.2). Figure 5 depicts the dimensionless components of the cation transport equation in various vertical positions.
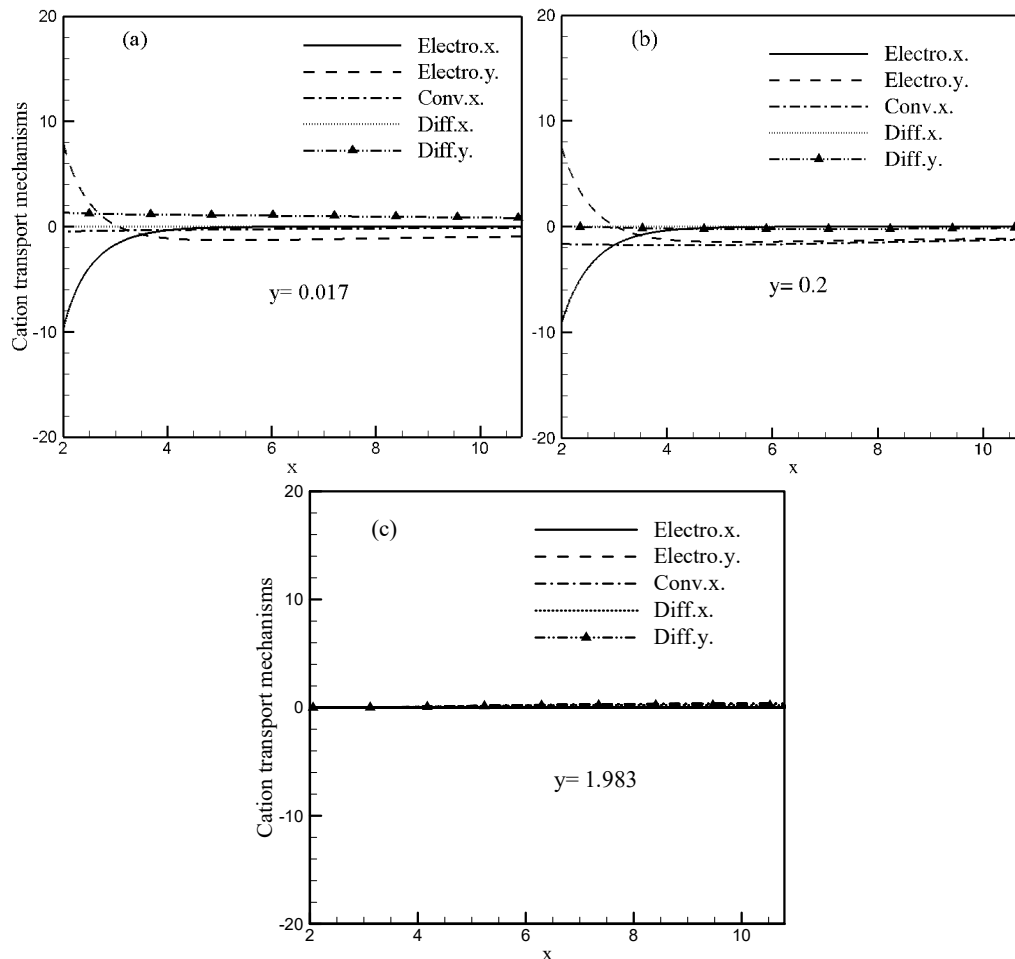

Figure 5. Dimensionless components of the cation transport equation terms at different vertical positions and after the electrode section. (a) y= 0.017, (b) y= 0.2, (c) y= 1.983

As seen in Fig. 5, the components at the vicinity of the upper wall (y=1.983) are almost negligible. It is seen that the repulsion of the co-ions (cations) from the anodic part (upper half) does not affect the near-wall downstream locations. However, in the vicinity of the lower wall (y= 0.017), components of the cation transport equation take non-negligible values. The x-component of the electro-migrative term (the attraction of counter-ions) becomes negligible at far downstream locations (i.e., x>4). However, the y component of the diffusive and electro-migrative terms remain non-negligible at all downstream locations and much bigger compared to the x-component of the convective term, since, close to the wall, the convective term diminishes significantly. A slow-diminishing trend is observed in the magnitude of the y-component of electro-migrative and diffusive terms in the vicinity of the lower-wall (cathodic half-cell) by approaching the outlet section and is expected to reach zero values if the exit section is sufficiently elongated.

At the middle of the lower half of the channel (y= 0.2) and by moving away from the electrode toward the channel outlet (x>4), all terms diminish except the y-component of the electro-migrative term and the x-component of the convective term. It is deduced that by moving away from the lower wall (cathodic part) toward the middle of the channel, the diffusion of cations (counter-ions) reduces tremendously.

Conclusions

A computational model is introduced to study the electrification mechanism and the electrohydrodynamic flow inside the electrostatic atomizers. The suggested model is applied to a microchannel with the electrode and insulated sections resembling the conditions inside the electrostatic atomizers. Realistic ionic boundary conditions are considered at the electrodes taking into account the counter-ions discharge based on the concurrent experimental measurements. The cation concentration along the channel is investigated at different vertical positions. Strong repulsion of cations from the anodic surface influences the concentration at downstream locations in upper-half of the channel significantly. It is observed that the diffusion from the lower half of the channel gradually replenishes the void area of cation concentration downstream of the electrode and in the upper half of the channel. The cation transport equation components are compared with each other along the electrically-insulated exit section of the microchannel. It is deduced that at downstream locations close to the wall, the diffusion of the counter-ions remains high. However, by moving away from the wall toward the center-line of the channel, the magnitude of the diffusion of counter-ions decreases significantly. The y-component of the electromigration of counter-ions (attraction) remains high at both close-to-the-wall and far-from-the-wall locations. By moving away from the electrode and approaching the outlet of the microchannel; both diffusive and electro-migrative terms start to decrease gradually. It is expected to observe zero values of diffusive and electro-migrative terms at the exit for sufficiently large exit-section lengths. The diffuse layer thickness is defined and indicated along the electrode section. It seems that the thickness of the diffuse layer is affected by the electrode length. In this study, the diffuse layer takes a concave configuration. It is expected to see a uniform diffuse-layer thickness along the length of the channel for higher ratios of the electrode length to the channel half-height.

Acknowledgements

Nomenclature
Roman Symbols

a_c	constant parameter
b_c	constant parameter
c_*^+	cation concentration [m^{-3}]
c_*^-	anion concentration [m^{-3}]
$c_{*\infty}$	bulk ion concentration [m^{-3}]
D	diffusivity coefficient [m^2 s^{-1}]
$\mathbf{E}_*$	electric field vector [V m^{-1}]
$\mathbf{E}_{*ext}$	externally applied electric field vector [V m^{-1}]
e	elementary charge [C]
H_*	channel height [m]
h_*	half channel height [m]
J_{e*}	electric current density [A m^{-2}]
$j_*^{\pm}$	ion flux [m^{-2} s^{-1}]
j_{0*}	exchange current density [A m^{-2}]
k_B	Boltzmann constant [m^2 kg s^{-2} K]

n_{tot} total number of grid points
p_* pressure [Pa]
q_* charge density [C m^{-3}]
T temperature [K]
V_{0*} electrode potential [V]
$\mathbf{V}_*$ velocity vector [m]
x_* coordinate [m]
Δx_* cell size in x_* direction [m]
y_* coordinate [m]
Δy_* cell size in y_* direction [m]
t_* time [s]

Greek Symbols

ε solvent relative dielectric permittivity
ε_0 vacuum permittivity [F m^{-1}]
ζ zeta potential [V]
λ_d diffuse layer thickness [m]
λ_D Debye screening length [m]
μ dynamic viscosity [kg m^{-1} s^{-1}]
ρ_* density [kg m^{-3}]
σ electric conductivity [S m^{-1}]
τ_c charge relaxation time [s^{-1}]
φ_* electric potential [V]

Other Symbols

$*$ dimensional variable
∇ gradient operator [m^{-1}]
∇^2 Laplacian operator [m^{-2}]

References

[1] Yule, A., Shrimpton, J.S., Watkins, A. P., Balachandran, W., Hu, D., 1995, Fuel, 74 (7), pp. 1094-1103.
[2] Kourmatzis, A., Shrimpton, J. S., 2009, Atomization and Sprays, 19 (11), pp. 1045-1063.
[3] Rigit, A. R. H., Shrimpton, J. S., 2006, Atomization and Sprays, 16 (4), pp. 401-419.
[4] Taylor, G., 1966, Proceedings of the Royal Society of London A, 291 (1425), pp. 159-166.
[5] Levich, V. G., 1962, "Physicochemical Hydrodynamics".
[6] Melcher, J. R., Taylor, G. I., 1969, Annual Review of Fluid Mechanics, 1 (1), pp. 111-146.
[7] Saville, D. A., 1977, Annual Review of Fluid Mechanics, 29 (1), pp. 27-64.
[8] Shrimpton, J. S., 2009, "Charge Injection Systems – Physical Principles, Experimental and Theoretical Work".
[9] Zhang, Y., Yarin, A. L., 2012, Journal of the Electrochemical Society, 159 (10), pp. 787-791.
[10] Sankaran, A., Staszel, C., Sahu, R. P., Yarin, A. L., Mashayek, F., 2017, Langmuir, 33 (6), pp. 1375-1384.
[11] Sankaran, A., Staszel, Yarin, A. L., Mashayek, F., 2018, Electrochimica Acta, 268, pp. 173-186.
[12] Bard, A. J., Faulkner, L. R., 2001, "Electrochemical Methods Fundamentals and Applications".
[13] Antropov, L. I., 2001, "Theoretical Electrochemistry".
[14] Frumkin, A., 1955, Z. Elektrochem, 59, pp. 807-822.
[15] Bonnefont, A., Argoul, F., Bazant, M., 2001, Journal of Electroanalytical Chemistry, 500, pp. 52-61.
[16] Stern, O., 1924, Z. Elektrochem, 30, pp. 508-516.
[17] Castellanos, A., Perez, A. T., 2007, Electrohydrodynamic Systems. In "Handbook of Experimental Fluid Mechanics".
[18] Perez, A. T., Traore, P., Koulova-Nenova, D., Romat, H., 2009, IEEE Transactions on Dielectrics and Electrical Insulation, 16 (2), pp. 448-455.
[19] Traore, P., Daaboul, M., Louste, C., 2010, Journal of Physics D: Applied Physics, 43, pp. 225502(1)-225502(8).
[20] Chu, K. T., Bazant, M. Z., 2005, SIAM Journal of Applied Mathematics, 65 (5), pp. 1485-1505.
[21] Bazant, M. Z., Chu, K. T., Bayly, B. J., 2005, SIAM Journal of Applied Mathematics, 65 (5), pp. 1463-1484.
[22] Weller, H. G., Tabor, G., Jasak, H., Fureby, C., 1998, Computers in Physics, 12, pp. 620-631.
[23] Perez, E. E., Carelli, A. A., Crapiste, G. H., 2011, Journal of Food Engineering, 105 (1), pp. 180-185.
[24] Karniadakis, G. E., Beskok, A., Aluru, N., 2015, "Microflows and Nanoflows Fundamentals and Simulation".
[25] Kashir, B., Perri, A., Yarin, A. L., Mashayek, F., 2019, Physics of Fluids, 31 (2), pp. 021201(1)-021201(17)
[26] Kashir, B., Perri, A., Schick, R. J., Yarin, A. L., Mashayek, F., July 22 - 26 2018, 14th Triennial International Conference on Liquid Atomization and Spray Systems.